First-principles theory of infrared vibrational spectroscopy of metals and semimetals: Application to graphite

Luca Binci [1,2,*] Paolo Barone [3] and Francesco Mauri [1,2]

[1] *Dipartimento di Fisica, Università di Roma La Sapienza, Piazzale Aldo Moro 5, I-00185 Roma, Italy*

[2] *Graphene Labs, Fondazione Istituto Italiano di Tecnologia, Via Morego, I-16163 Genova, Italy*

[3] *SPIN-CNR, c/o Università G. D'Annunzio, I-66100 Chieti, Italy*

(Received 28 January 2021; accepted 17 March 2021; published 13 April 2021)

We develop an *ab initio* method to simulate the infrared vibrational response of metallic systems in the framework of time-dependent density functional perturbation theory. By introducing a generalized frequency-dependent Born effective charge tensor, we show that phonon peaks in the reflectivity of metals can always be described by a Fano function, whose shape is determined by the complex nature of the frequency-dependent effective charges and electronic dielectric tensor. The IR vibrational properties of graphite, chosen as a representative test case to benchmark our method, are found to be accurately reproduced. Our approach offers a first-principles scheme for the prediction and understanding of IR reflectance spectra of metals, which may represent one of the few available tools of investigation of these materials when subjected to extremely high-pressure conditions.

DOI: 10.1103/PhysRevB.103.134304

I. INTRODUCTION

Infrared (IR) spectroscopy is a well-established technique for analyzing the vibrational properties of crystalline solids. In insulating or semiconducting materials, not displaying electronic intraband transitions in the IR region of the electromagnetic spectrum, phonon features arise at energies much smaller than the band gap, and hence they can be clearly identified. On the other hand, the IR response in metals is dominated by the Drude peak—the signature of the free electron response—whose amplitude is proportional to the free carrier density ρ, and therefore to the square of the plasma frequency $\rho \propto \omega_p^2$. The presence of a strong Drude peak generally precludes the detection of the vibrational features [1]. There are cases, however, in which this technique can also be useful in metallic materials, and even situations in which it is one of the only possible choices. To better understand these cases, it is useful to recall the quantum-mechanical dependence of ω_p from the density of states at the Fermi level, $D(E_F)$, and the average electronic velocity at the Fermi surface, $\bar{v}_F$: $\omega_p^2 \propto \bar{v}_F^2 D(E_F)$. From this expression it is clear that, for example, systems with a pseudogap—like high-temperature superconducting cuprates [2] or transition-metal dichalcogenides undergoing a charge-density-wave transition [3–5]—displaying by definition a density of states that decreases significantly at the Fermi level, will have a small ω_p; this condition narrows the Drude peak, and it makes the vibrational features sharp enough to be investigated (see, e.g., Fig. 1 of Ref. [6], or Fig. 1 of Ref. [7]). Another significant example is given by systems under extremely high-pressure conditions, i.e., above hundreds of GPa, like H_3S [8,9], LaH_{10} [10,11], and the recently discovered semimetallic phase of hydrogen [12]. For these systems, the experiments in order to be performed require a setup composed of diamond anvil cells, and samples whose size is of the order of μm. For the determination of the crystal structure, the reduced sample size and the diamond-anvil environment—together with the presence of a light element like hydrogen—preclude the use of neutron scattering, and this makes an x-ray diffraction analysis very challenging [9,13]. Raman and IR spectroscopies represent alternative routes to this goal. However, Raman spectroscopy of metals turns out to be difficult because of the smallness of the light penetration depth within the sample, $\delta \propto (\omega\sigma_0)^{-1/2}$, for ω in the visible light and high dc conductivity σ_0. Therefore, due to the lower frequencies employed, IR reflectivity measurements represent one of the few possible and effective approaches for investigating the crystal structure of metallic materials under extremely high-pressure conditions [9].

II. THEORY

Ab initio calculations play a crucial role in the physical interpretation of experimental results. In this paper, by means of a time-dependent formulation of density functional perturbation theory (DFPT) [14,15], we introduce a method to simulate from first principles the IR reflectivity absorption spectrum of metallic systems.

The determination of the dielectric tensor $\boldsymbol{\epsilon}(\omega)$ gives a complete characterization of all the features appearing in IR spectra [16–18]. It can be decomposed as

$$\boldsymbol{\epsilon}(\omega) = \boldsymbol{\epsilon}^{e}(\omega) + 4\pi \sum_s \boldsymbol{\chi}_s^{I}(\omega), \tag{1}$$

*Present address: École Polytechnique Fédérale de Lausanne (EPFL), Station 9, CH-1015 Lausanne, Switzerland.

where $\boldsymbol{\epsilon}^{\mathrm{e}}(\omega)$ is the electronic dielectric tensor at fixed ions, and $\boldsymbol{\chi}^{\mathrm{I}}_s(\omega)$ represents the ionic contribution due to a phonon mode with index s,

$$\boldsymbol{\chi}^{\mathrm{I}}_s(\omega) = \frac{e^2}{\Omega}\,\frac{\mathbf{d}_s(\omega)\,\mathbf{d}_s(\omega)}{\omega_s^2 - (\omega + i\gamma_s/2)^2}. \tag{2}$$

Here, Ω is the unit-cell volume, ω_s and γ_s are the phonon frequency and inverse lifetime, respectively, and $\mathbf{d}_s(\omega) = \sum_\kappa \mathbf{Z}_\kappa(\omega)\cdot\frac{\mathbf{e}_{s,\kappa}}{\sqrt{m_\kappa}}$ is the oscillator strength defined in terms of a frequency-dependent effective charge tensor $\mathbf{Z}_\kappa(\omega)$, with m_κ the mass of the κth atom and $\mathbf{e}_{s,\kappa}$ the polarization vector of the sth mode. Equations (1) and (2) can be derived either by a phenomenological approach [16], or with more rigorous field-theoretic methods [17,18]. Since phonon peaks are typically rather sharp, we can approximate $\boldsymbol{\epsilon}^{\mathrm{e}}(\omega)$ and $\mathbf{Z}_\kappa(\omega)$ by their values $\boldsymbol{\epsilon}^{\mathrm{e}}_s = \boldsymbol{\epsilon}^{\mathrm{e}}(\omega_s)$ and $\mathbf{Z}_\kappa(\omega_s)$ at each given phonon mode s.

Information from IR studies are generally extracted from transmission $T(\omega)$ and reflectivity $R(\omega)$ measurements. In the case of metals, $T(\omega)$ can be obtained only for very thin materials, whereas $R(\omega)$ can always be acquired. The standard formula of the reflectivity between the vacuum and the sample along one of the principal dielectric axes α is $R_\alpha(\omega) = \left|\frac{\sqrt{\epsilon_\alpha(\omega)}-1}{\sqrt{\epsilon_\alpha(\omega)}+1}\right|^2$ [1], where $\epsilon_\alpha(\omega)$ is the diagonal element of the dielectric tensor. The general shape of the vibrational features in IR reflectivity spectra of metals can be deduced by a Taylor expansion of $R_\alpha(\omega)$ around a given s phonon mode. In the limit $|\epsilon^{\mathrm{e}}_{s,\alpha}| \gg |\chi^{\mathrm{I}}_{s,\alpha}(\omega)|$, the reflectivity reads (see Appendix A)

$$R_{s,\alpha}(\omega) \sim R^{\mathrm{e}}_{s,\alpha}\left[1 + 2\,\mathrm{Re}\left(\frac{4\pi\,\chi^{\mathrm{I}}_{s,\alpha}(\omega)}{\sqrt{\epsilon^{\mathrm{e}}_{s,\alpha}}\left(\epsilon^{\mathrm{e}}_{s,\alpha}-1\right)}\right)\right]. \tag{3}$$

where $R^{\mathrm{e}}_{s,\alpha}$ is the purely electronic reflectivity. The vibrational contribution (second term in the square brackets) can be recast as a Fano profile,

$$\mathrm{Re}\left(\frac{4\pi\,\chi^{\mathrm{I}}_{s,\alpha}(\omega)}{\sqrt{\epsilon^{\mathrm{e}}_{s,\alpha}}\left(\epsilon^{\mathrm{e}}_{s,\alpha}-1\right)}\right) = W_{s,\alpha}\,\frac{q^2_{s,\alpha} - 1 + 2q_{s,\alpha}\,\xi_s(\omega)}{\left(1+q^2_{s,\alpha}\right)\left(1+\xi^2_s(\omega)\right)}. \tag{4}$$

Here we defined the following quantities:

$$W_{s,\alpha} = \frac{|D_{s,\alpha}|^2}{\gamma_s\omega_s}, \qquad q_{s,\alpha} = -\frac{\mathrm{Re}\,D_{s,\alpha}}{\mathrm{Im}\,D_{s,\alpha}}, \tag{5}$$

$$(D_{s,\alpha})^2 = i\,\frac{4\pi e^2}{\Omega}\,\frac{(d_{s,\alpha})^2}{\sqrt{\epsilon^{\mathrm{e}}_{s,\alpha}}\left(\epsilon^{\mathrm{e}}_{s,\alpha}-1\right)}, \tag{6}$$

whereas $\xi_s(\omega) = (\omega^2 - \omega_s^2)/\gamma_s\omega$, which, close to a phonon peak, can be approximated to $\xi_s(\omega) \sim 2(\omega-\omega_s)/\gamma_s$. Equation (4) is a Fano function in the variable $\xi_s(\omega)$ [19], which is completely determined by five parameters, namely R^{e}_s, ω_s, γ_s, $W_{s,\alpha}$, and $q_{s,\alpha}$. This implies that, in the case of metals, it cannot be used to obtain all six parameters characterizing $\boldsymbol{\epsilon}(\omega)$, i.e., $(\mathrm{Re}\,\mathbf{Z}_\kappa, \mathrm{Im}\,\mathbf{Z}_\kappa)$, $(\mathrm{Re}\,\boldsymbol{\epsilon}^{\mathrm{e}}_s, \mathrm{Im}\,\boldsymbol{\epsilon}^{\mathrm{e}}_s)$, γ_s, ω_s [9,20]. Instead, the proper way to obtain both the real and the imaginary parts of $\mathbf{Z}_\kappa$ is to fit the vibrational contribution of the real part of the optical conductivity; this can be done once the smooth electronic part has been previously subtracted, as was done, e.g., in Ref. [21]. The reflectivity expansion in Eqs. (3) and (4) holds for every material, both metallic and insulating. Indeed, for $\mathrm{Im}\,\mathbf{Z}_\kappa \to \mathbf{0}$ ($q_{s,\alpha} \to -\infty$) one recovers the standard insulating limit of a Lorentzian shape. For metals instead, as static polarization is not a well-defined quantity, the effective charge can only be defined in the dynamical (ω-dependent) version. We show that its imaginary part is responsible for the Fano shape of the phonon peaks in reflectivity spectra.

In DFPT, both $\boldsymbol{\epsilon}^{\mathrm{e}}$ and $\mathbf{Z}_\kappa$ are defined as derivatives of the electronic polarization, the former with respect to the electric field $\mathbf{E}$, the latter with respect to the ionic displacements $\mathbf{u}_\kappa$ [22]. The effective charge tensor can be decomposed in two contributions $\mathbf{Z}_\kappa = \mathbf{1}Z^{\mathrm{I}}_\kappa + \mathbf{Z}^{\mathrm{e}}_\kappa$, where the first (constant) term Z^{I}_κ is the (pseudo)charge of the nuclei, while the second electronic contribution $\mathbf{Z}^{\mathrm{e}}_\kappa$ is due to the interaction between the electrons and the lattice; in the following, we will focus on this last one. Within time-dependent DFPT [14,15] and adopting the variational approach proposed in [23], the effective charge tensor can be expressed as

$$\begin{aligned} e\mathbf{Z}^{\mathrm{e}}_\kappa[n^{\mathbf{E}}, n^{\mathbf{u}_\kappa}](\omega_s) = &-\frac{2}{N_{\mathbf{k}}}\sum_{\mathbf{k},nm}\frac{f_{\mathbf{k},n} - f_{\mathbf{k},m}}{(E_{\mathbf{k},n} - E_{\mathbf{k},m})^2 - z_s^2}\langle u_{\mathbf{k},m}|\left(ie\hbar\mathbf{v}_{\mathbf{k}} + (E_{\mathbf{k},n} - E_{\mathbf{k},m})V^{\mathbf{E}}_{\mathrm{Hxc}}\right)|u_{\mathbf{k},n}\rangle\langle u_{\mathbf{k},n}|\left(V^{\mathbf{u}_\kappa}_{\mathrm{I}} + V^{\mathbf{u}_\kappa}_{\mathrm{Hxc}}\right)|u_{\mathbf{k},m}\rangle \\ &+ \int d^3r\,d^3r'\,n^{\mathbf{E}}(\mathbf{r},\omega_s)\,K_{\mathrm{Hxc}}(\mathbf{r},\mathbf{r}')\,n^{\mathbf{u}_\kappa}(\mathbf{r}',\omega_s), \end{aligned} \tag{7}$$

while the electronic dielectric tensor $\boldsymbol{\epsilon}^{\mathrm{e}}(\omega_s)$ reads

$$\begin{aligned} \boldsymbol{\epsilon}^{\mathrm{e}}[n^{\mathbf{E}}](\omega_s) = \mathbf{1} + 4\pi\,&\frac{2}{N_{\mathbf{k}}\Omega}\sum_{\mathbf{k},nm}\frac{1}{(E_{\mathbf{k},n} - E_{\mathbf{k},m})^2 - z_s^2}\,\frac{f_{\mathbf{k},n} - f_{\mathbf{k},m}}{E_{\mathbf{k},n} - E_{\mathbf{k},m}}\langle u_{\mathbf{k},m}|\left(ie\hbar\mathbf{v}_{\mathbf{k}} + (E_{\mathbf{k},n} - E_{\mathbf{k},m})V^{\mathbf{E}}_{\mathrm{Hxc}}\right)|u_{\mathbf{k},n}\rangle \\ &\times\langle u_{\mathbf{k},n}|\left(ie\hbar\mathbf{v}_{\mathbf{k}} + (E_{\mathbf{k},m} - E_{\mathbf{k},n})V^{\mathbf{E}}_{\mathrm{Hxc}}\right)|u_{\mathbf{k},m}\rangle + \frac{4\pi}{\Omega}\int d^3r\,d^3r'\,n^{\mathbf{E}}(\mathbf{r},\omega_s)\,K_{\mathrm{Hxc}}(\mathbf{r},\mathbf{r}')\,n^{\mathbf{E}}(\mathbf{r}',\omega_s). \end{aligned} \tag{8}$$

In these expressions, $N_{\mathbf{k}}$ is the number of points in the $\mathbf{k}$-grid, $\mathbf{v}_{\mathbf{k}} = \frac{1}{\hbar}\frac{\partial H^0_{\mathbf{k}}}{\partial\mathbf{k}}$, where $H^0_{\mathbf{k}} = e^{-i\mathbf{k}\cdot\mathbf{r}}H^0e^{i\mathbf{k}\cdot\mathbf{r}}$, and H^0 is the unperturbed Kohn-Sham (KS) Hamiltonian; $E_{\mathbf{k},n}$ is the unperturbed KS eigenvalue, and $u_{\mathbf{k},n}$ is the periodic part of the corresponding KS eigenstate in Bloch form [24]. We denote with $f_{\mathbf{k},n}$ the smearing function, while $z_s = \hbar\omega_s + i\eta_s$, where

η_s is a positive small real number with the dimension of an energy. The frequency-dependent charge density induced by $\boldsymbol{\xi} = \mathbf{E}, \mathbf{u}_\kappa$, denoted as $n^{\boldsymbol{\xi}} = \frac{\partial n}{\partial \boldsymbol{\xi}}$, gives rise to a Hartree and exchange-correlation (Hxc) potential:

$$V^{\boldsymbol{\xi}}_{\mathrm{Hxc}}\big[n^{\boldsymbol{\xi}}\big](\mathbf{r}, \omega_s) = \int d^3 r\, K_{\mathrm{Hxc}}(\mathbf{r}, \mathbf{r}')\, n^{\boldsymbol{\xi}}(\mathbf{r}', \omega_s), \tag{9}$$

where $K_{\mathrm{Hxc}}(\mathbf{r}, \mathbf{r}') = \frac{\delta^2 E_{\mathrm{Hxc}}[n]}{\delta n(\mathbf{r}) \delta n(\mathbf{r}')}$ is the Hxc kernel. Finally, the first-order perturbative expressions of the induced charge density with respect to the electric field and ionic displacements are

$$n^{\mathbf{E}}(\omega_s) = \frac{2}{N_{\mathbf{k}}} \sum_{\mathbf{k},nm} \frac{f_{\mathbf{k},n} - f_{\mathbf{k},m}}{(E_{\mathbf{k},n} - E_{\mathbf{k},m})^2 - z_s^2}\, u^*_{\mathbf{k},n}\, u_{\mathbf{k},m} \times \langle u_{\mathbf{k},m} | \big(ie\hbar \mathbf{v}_{\mathbf{k}} + (E_{\mathbf{k},n} - E_{\mathbf{k},m}) V^{\mathbf{E}}_{\mathrm{Hxc}} \big) | u_{\mathbf{k},n} \rangle \tag{10}$$

and

$$n^{\mathbf{u}_\kappa}(\omega_s) = \frac{2}{N_{\mathbf{k}}} \sum_{\mathbf{k},nm} \frac{f_{\mathbf{k},n} - f_{\mathbf{k},m}}{(E_{\mathbf{k},n} - E_{\mathbf{k},m})^2 - z_s^2}\, u^*_{\mathbf{k},n}\, u_{\mathbf{k},m} \times (E_{\mathbf{k},n} - E_{\mathbf{k},m}) \langle u_{\mathbf{k},m} | \big(V^{\mathbf{u}_\kappa}_{\mathrm{I}} + V^{\mathbf{u}_\kappa}_{\mathrm{Hxc}} \big) | u_{\mathbf{k},n} \rangle. \tag{11}$$

To highlight certain analytical properties, we wrote the previous expressions in a slightly different way with respect to their standard form [23]. It is clear that only $\lim_{z\to 0} n^{\mathbf{u}_\kappa}$ is in general well-defined: in the limit of infinite $\mathbf{k}$ points, all the other quantities have an integrand that can become arbitrarily large when $z \to 0$ if the Fermi level falls between the intersection of two bands $(\tilde{m}, \tilde{n})$ at a point $\mathbf{k}^*$, where $\lim_{\mathbf{k}\to\mathbf{k}^*} E_{\mathbf{k},\tilde{n}} - E_{\mathbf{k},\tilde{m}} \to 0$. Note that—contrary to the induced charge densities, Eqs. (10) and (11), and the effective charge tensor, Eq. (7)—only $\boldsymbol{\epsilon}^{\mathrm{e}}$ contains a contribution from intraband terms, which is always divergent when $z \to 0$ and gives rise to the Drude peak. It is therefore necessary to maintain the frequency dependence of all relevant quantities—namely, $n^{\boldsymbol{\xi}}$, $\boldsymbol{Z}^{\mathrm{e}}_\kappa$, and $\boldsymbol{\epsilon}^{\mathrm{e}}$—in order to have a stable and robust implementation of Eqs. (7), (8), and (10) in a first-principles code.

Although feasible in principle, a full implementation would require a substantial rewriting of the linear-response code. Therefore, for computational simplicity, we exploit the variational property with respect to the first-order charge density of Eqs. (7) and (8) (as discussed in Ref. [23]), neglecting in all the self-consistent loops the imaginary part of the first-order charge density:

$$\boldsymbol{Z}^{\mathrm{e}}_\kappa(\omega_s) \approx \boldsymbol{Z}^{\mathrm{e}}_\kappa\big[\mathrm{Re}\, n^{\mathbf{E}}, \mathrm{Re}\, n^{\mathbf{u}_\kappa}\big](\omega_s), \tag{12}$$

$$\boldsymbol{\epsilon}^{\mathrm{e}}(\omega_s) \approx \boldsymbol{\epsilon}^{\mathrm{e}}\big[\mathrm{Re}\, n^{\mathbf{E}}\big](\omega_s). \tag{13}$$

Regarding the practical implementation in the code, we used a dynamical extension of the linear-response formalism described in Ref. [15], which is equivalent to the one of Ref. [23], employing a frequency-dependent Sternheimer equation with a similar scheme of Ref. [25] (see Appendix B for more details).

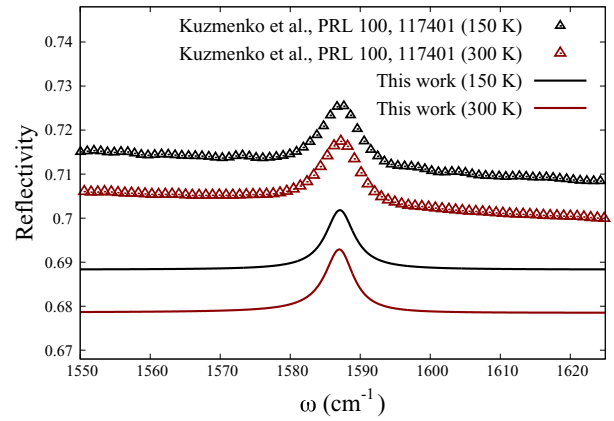

FIG. 1. Simulated (lines) and experimental (dots) phonon peak associated with the E_{1u} mode. We shifted the experimental peaks so that their tips are at 1587 cm^{-1}.

III. APPLICATIONS

A. Graphite

We benchmark our approach by evaluating the reflectivity spectra of bulk graphite and analyzing the IR peaks E_{1u} ($\omega_{E_{1u}} = 1587$ cm^{-1}) and A_{2u} ($\omega_{A_{2u}} = 868$ cm^{-1}), which have been thoroughly investigated by IR spectroscopy measurements [20,26–34]. Lattice symmetry forces tensorial quantities to be diagonal, and the in-plane elements to be equal. In the following, we will denote as $T_\parallel$ ($T_\perp$) the components of a given tensor $\boldsymbol{T}$ parallel (perpendicular) to the graphene sheets. *Ab initio* calculations were performed using the PW and PHonon packages of QUANTUM ESPRESSO [35,36], within which we implemented the theory described above. We use the local-density approximation [37], norm-conserving pseudopotentials [38], Fermi-Dirac smearing, and a plane-wave expansion up to 55 Ry cutoff. We choose the value of η_s to be one order of magnitude smaller than the corresponding ω_s values: $\eta_{E_{1u}} = 110$ cm^{-1} and $\eta_{A_{2u}} = 55$ cm^{-1}. We account for the thermal expansion using as a lattice constant $c = 6.68$ Å for $T = 150$ K and $c = 6.70$ Å for $T = 300$ K, while keeping the in-plane lattice constant fixed at $a = 2.46$ Å [39]. We use as ω_s the values taken from Ref. [20]. Regarding the $\mathbf{k}$-point sampling, as graphene, bulk graphite is a semimetal with valence and conduction bands touching and crossing at the high-symmetry $\mathbf{K}$ and $\mathbf{H}$ points in the Brillouin zone, so interband electronic transitions will contribute to the optical response for any value of $\hbar\omega$. At IR frequencies, the most significant contributions to the E_{1u} absorption come from a small cylinder along the $\mathbf{K}$-$\mathbf{H}$ line, in which the denominators in Eqs. (7) and (8) reach their minimum value. Thus, a very fine $\mathbf{k}$-points grid around this region is needed for an accurate evaluation of the sum over $\mathbf{k}$ appearing in Eqs. (7) and (8). To this end, we employed a mesh with a uniform sampling along the k_z direction, and a nonuniform grid within the (k_x, k_y) plane, where the density of $\mathbf{k}$-points increases exponentially around the $\mathbf{K}$-$\mathbf{H}$ line obeying a C_3 symmetry (details can be found in Appendix C).

In Figs. 1 and 2 we compare our simulated reflectivity with the experimental data. Importantly, we notice that the symmetry of the peaks depends on the phases of both $\boldsymbol{Z}_\kappa(\omega_s)$

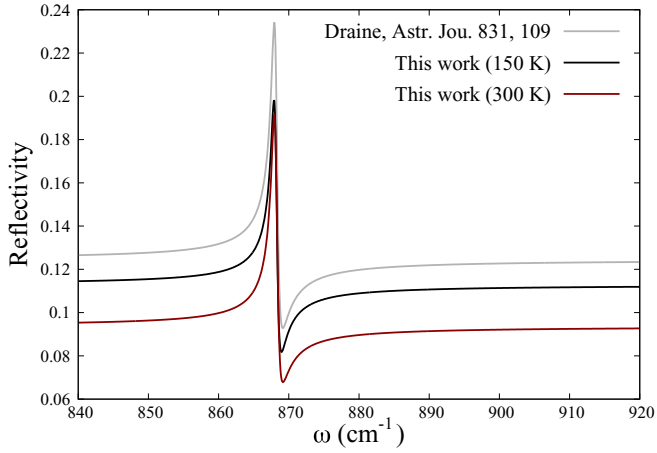

FIG. 2. Comparison between our *ab initio* results (black and red lines) and a fit (whose parameters are not related to a particular T) taken from Ref. [34] (gray line) of the reflectivity around the resonance of the A_{2u} mode.

and $\boldsymbol{\epsilon}^{\mathrm{e}}(\omega_s)$. In fact, from Eq. (6), $D_{s,\alpha} = |D_{s,\alpha}|e^{i \arg D_{s,\alpha}}$, where for $|\epsilon^{\mathrm{e}}_{s,\alpha}| \gg 1$, $\arg D_{s,\alpha} \approx \frac{\pi}{4} + \arg d_{s,\alpha} - \frac{3}{4} \arg \epsilon^{\mathrm{e}}_{s,\alpha}$, and from Eq. (5), $\tan(\arg D_{s,\alpha}) = -\frac{1}{q_{s,\alpha}}$. Using our computed values in Tables I and II, for the E_{1u} peak (Fig. 1) we find $q_{E_{1u},\parallel} \approx -52\,(-19)$ at $T = 150\,(300)$ K ($q \ll -1$ is the Lorentzian limit), which explains the symmetric shape of the resonance. Remarkably, the temperature dependence obtained from our calculations—mainly due to the temperature dependence of $\boldsymbol{\epsilon}^{\mathrm{e}}(\omega_s)$—well reproduces the one reported in Ref. [30]. As for the A_{2u} peak, we compare the calculated $R_\perp(\omega)$ with a fit proposed in Ref. [34] and realized taking into account several experiments. As shown in Fig. 2, also in this case our approach successfully reproduces the expected Fano asymmetric shape of the phonon peak, for which $q_{A_{2u},\perp} \approx -1.3\,(-1.4)$ at $T = 150\,(300)$ K ($q = -1$ is the complete asymmetric case).

We report in Table I the oscillator strengths $d_\perp$ ($d_\parallel$) of Eq. (2) evaluated at $\omega_{E_{1u}}$ ($\omega_{A_{2u}}$) and properly rescaled by the square root of the carbon mass m_{C} (and a factor 2 stemming from the scalar product with the polarization vectors $\mathbf{e}_{s,\kappa}$),

TABLE I. Comparison between *ab initio* and experimental/theoretical oscillator strength $\tilde{\mathbf{d}}_s = \sqrt{m_{\mathrm{C}}/4}\,\mathbf{d}_s$. The parallel component refers to the E_{1u} mode, the perpendicular one to the A_{2u} mode.

Reference	T (K)	Re $\tilde{d}_\parallel$	Im $\tilde{d}_\parallel$	Re $\tilde{d}_\perp$	Im $\tilde{d}_\perp$
Ref. [20][b]		0.41		0.08	
Ref. [27][b]	300	0.18			
Ref. [28][b]	300	0.21			
Ref. [40][a]		0.014	0.015		
Ref. [26][a]	150	0.17	0.15		
	300	0.18	0.15		
Ref. [26][b]	150	0.29	0.14		
	300	0.31	0.13		
Present work	150	0.27	0.09	0.07	0.0001
	300	0.27	0.10	0.07	0.0001

[a]Theoretical
[b]Experimental.

TABLE II. Comparison between *ab initio* and experimental dielectric tensor. For comparison, we also report the value of Re $\epsilon_\perp$ at $\omega = 9679$ cm^{-1} (taken from Ref. [33]) because, although it is not the characteristic frequency of the A_{2u} mode, the dielectric tensor is not expected to vary appreciably from 686 to 9679 cm^{-1} since there are no interband electronic transitions in such a frequency range.

Reference	T (K)	Re $\epsilon_\parallel$	Im $\epsilon_\parallel$	Re $\epsilon_\perp$	Im $\epsilon_\perp$
Ref. [29][a]		8.8	50		
Ref. [31][a]		0.73	73		
Ref. [32][a]				5.3	0.68
Ref. [33][a]				3.3	
Ref. [34][b]				4.2	0.89
Present work	150	6.1	62	3.9	0.79
	300	7.9	59	3.4	0.71

[a]As reported by Ref. [34].
[b]Values corresponding to a fit realized taking into account many experimental data.

and we compare them with available experimental estimates. In the case of graphite, they are equal to the average of the absolute value of $Z_\parallel$ ($Z_\perp$) of the four C atoms of the unit cell, which, because of symmetry, are exactly equal in pairs, with opposite sign. In addition, it is well known that the components of the effective charge tensor obey the acoustic sum rule (ASR) $\sum_\kappa \boldsymbol{Z}_\kappa = \mathbf{0}$ [16]; interestingly, we found that this rule in general is not respected in the dynamical case (see Table V in Appendix D).

We stress the fact that in older experiments, the effective charge was supposed to be a real quantity, and the imaginary part was completely neglected [20,27,28], an assumption that has been relaxed only recently [26]. Such neglect of the complex nature of the effective charges may have led to inaccurate results because of a wrong fitting procedure of the experimental data. Within our approach, we find that indeed the imaginary part of $d_\parallel$ is approximatively 1/3 of the real part, in good agreement with the experimental results reported in Ref. [26]. The out-of-plane component $d_\perp$ has a negligible imaginary part, whereas the real one is found to be one order of magnitude smaller than Re $d_\parallel$ (reflecting the dielectric-like properties of graphite in the transverse direction), with our calculations yielding a value in excellent agreement with the experimental estimates [20]. We find that the combined effect of the thermal lattice expansion and the increase of electronic temperature has no effect on Re $d_\parallel$ and $d_\perp$. Instead, Im $d_\parallel$ does not depend appreciably on thermal expansion, but it increases with T, contrary to Ref. [26]. However, it is worth mentioning that the parameter $\eta_s = \mathrm{Im}\, z_s$, accounting for the damping of the electronic states, is also T-dependent. We have not studied such a dependence; nevertheless, in Appendix D we show that the variation of η_s can markedly affect Im $d_\parallel$.

As for the electronic dielectric tensor $\boldsymbol{\epsilon}^{\mathrm{e}}(\omega_s)$, in Table II we report $\epsilon_\parallel$ ($\epsilon_\perp$) evaluated at $\omega_{E_{1u}}$ ($\omega_{A_{2u}}$). We found that the components of the dielectric tensor depend only on the electronic temperature and not on the lattice thermal expansion. Also for $\boldsymbol{\epsilon}^{\mathrm{e}}(\omega_s)$, as well as for $\boldsymbol{Z}_\kappa(\omega_s)$, the in-plane components are always larger than the out-of-plane ones, both for the real and the imaginary parts. This is a consequence of the mirror

reflection symmetry with respect to the carbon planes, which is exact in monolayers like graphene, and only approximate in graphite, which forbids low-energy electronic excitations for perturbations perpendicular to the layered structure in the linear-response regime.

We finally mention that we also computed the nonadiabatic/adiabatic phonon frequencies for graphite (see the next section), finding $\omega_{E_{2g}}^{\mathrm{NA(A)}} = 1560.8\,(1560.5)$ cm^{-1} and $\omega_{E_{1u}}^{\mathrm{NA(A)}} = 1567.8\,(1569.4)$ cm^{-1} at $T = 300$ K; this gives a nonadiabatic (adiabatic) splitting of 7 (9) cm^{-1}, which compares well with the experimental splitting of 7 cm^{-1} at the same temperature [41].

B. Graphene bilayer and trilayers

As additional benchmarks, in this part we discuss the application of our theory to two related systems: graphene bilayer and the two types of graphene trilayer, with Bernal (ABA) and rhombohedral (ABC) stacking. Since, to the best of our knowledge, direct reflectivity experimental data are currently not available for these materials, we focus here on the effective charge tensor. Moreover, together with the oscillator strengths $\mathbf{d}_s$, we have also calculated both the adiabatic (ω_{A}) and nonadiabatic (ω_{NA}) optical phonon frequencies at $\mathbf{q} = \mathbf{\Gamma}$. To perform these last calculations, we modified the `ph.x` code of QUANTUM ESPRESSO in order to compute ω_{NA} at the $\mathbf{\Gamma}$ point of the BZ. The specific form of the finite-frequency generalized dynamical matrix at $\mathbf{q} = \mathbf{\Gamma}$ is analogous to Eq. (7), with the electric-field matrix elements replaced by the electron-phonon ones, and it is obtained using the same variational formulation and the same approximation of the charge density (i.e., the neglect of the imaginary part of the induced charge density) as for the effective charge and the dielectric tensors. This represents the same formulation as in Ref. [23], but at variance with that, we retained the frequency dependence in the first-order charge density, and we calculate explicitly the double counting term [see the second term of Eq. (B1) in Appendix B].

At variance with graphite, a splitting of in-plane and out-of-plane optical modes occurs in trilayer graphene. For the ABA stacking, such splitting involves the IR-active modes E_{1u} and A_{2u}: $E_{1u} \to E'_{(1)}, E'_{(2)}$, and $A_{2u} \to A''_{(1)}, A''_{(2)}$ for the out-of-plane mode. The $E'_{(1)}, E'_{(2)}$ modes of ABA trilayer graphene are also Raman-active. For the ABC stacking instead, the splitting affects only the Raman-active modes E_{2g} and B_{1g}: $E_{2g} \to E_g^{(1)}, E_g^{(2)}$ for the in-plane mode, and $B_{1g} \to A_{1g}^{(1)}, A_{1g}^{(2)}$ for the out-of-plane mode. For the bilayer, the splittings are analogous to those of graphite.

In Tables III and IV we show the results of our calculations. The temperature was set to 300 K for all the simulations, and we used the same lattice parameter and interlayer spacings of graphite at the same temperature. The adaptive **k**-point grid with parameters $(L, l, \mathcal{N}) = (10, 4, 25)$ and 1 N_{k_z} was used (see Appendix C), and all other computational details (pseudopotential, cutoff, etc.) are the same as for graphite.

For bilayer graphene, we compare our results with the experimental and theoretical data of Ref. [30]. Although our results are not precise as for graphite, they still represent a considerable improvement compared to the theoretical model employed in the same work. We point out that the quantitative discrepancy with the experimental results may also arise from the technical difficulties inherent in reflectivity measurements in bottom-gated bilayer graphene. Moreover, with our method we are also able to calculate the out-of-plane oscillator strength, a quantity that to our knowledge has never been computed for multilayered graphene. We have also evaluated the static limit of the effective charge tensor for the bilayer, yielding a value $\lim_{\omega\to 0} \tilde{d}_{\parallel}(\omega) = 0.349$. This is in good agreement with a theoretical value of 0.394 [17], obtained as the averaged limit of the zero electric field perpendicular to the graphene planes. Our calculated in-plane nonadiabatic phonon frequencies are very close to the adiabatic ones, in close analogy with the negligible nonadiabatic effect found in pristine graphite [42]. For the out-of-plane phonon frequencies, the inclusion of the ω-dependence induces a variation smaller than cm^{-1}, which is in fact practically negligible.

The calculated oscillator strengths and adiabatic/nonadiabatic frequencies for the two trilayers are reported in Table IV. In Fig. 3 we compare our results with experimental measurements from Ref. [43], showing the real part of the ionic conductivity $\boldsymbol{\sigma}^{\mathrm{ion}}(\omega)$ associated with the in-plane IR modes in units of $\pi e^2/(2h)$, linked to the

TABLE III. Bilayer. The oscillator strengths are $\tilde{\mathbf{d}}_s = \sqrt{m_C/4}\,\mathbf{d}_s$.

	E_g [a]	E_u [b]	A_g [a]	A_u [b]	Expt. [21]	Theor. [21]
Re $\tilde{d}_{\parallel}$		0.211			0.337 ± 0.113	0
Im $\tilde{d}_{\parallel}$		0.104				
$q_{\parallel}$		-2.029			-0.788 ± 0.298	
Re $\tilde{d}_{\perp}$				0.013		
Im $\tilde{d}_{\perp}$				-0.001		
ω_{A} (cm^{-1})	1561	1567	892	894		
ω_{NA} (cm^{-1})	1560	1565	892	894		

[a]Raman-active.
[b]IR-active.

TABLE IV. Trilayer Bernal ABA (top) and rhombohedral ABC (bottom). The oscillator strengths are $\tilde{\mathbf{d}}_s = \sqrt{m_C/6}\,\mathbf{d}_s$.

Bernal (ABA)	$E'_{(1)}$ [a,b]	$E'_{(2)}$ [a,b]	E'' [a]	$A''_{(1)}$ [b]	A' [a]	$A''_{(2)}$ [b]
Re $\tilde{d}_{\parallel}$	0.023	0.242				
Im $\tilde{d}_{\parallel}$	0.162	0.118				
Re $\tilde{d}_{\perp}$				0.013		0.015
Im $\tilde{d}_{\perp}$				-0.002		-0.003
ω_{A} (cm^{-1})	1563	1564	1570	888	893	893
ω_{NA} (cm^{-1})	1563	1566	1569	888	893	893

Rhombohedral (ABC)	$E_g^{(1)}$ [a]	E_u [b]	$E_g^{(2)}$ [a]	$A_g^{(1)}$ [a]	A_u [b]	$A_g^{(2)}$ [a]
Re $\tilde{d}_{\parallel}$		0.207				
Im $\tilde{d}_{\parallel}$		0.055				
Re $\tilde{d}_{\perp}$					0.011	
Im $\tilde{d}_{\perp}$					-0.002	
ω_{A} (cm^{-1})	1563	1567	1571	888	893	893
ω_{NA} (cm^{-1})	1561	1563	1570	888	893	893

[a]Raman-active.
[b]IR-active.

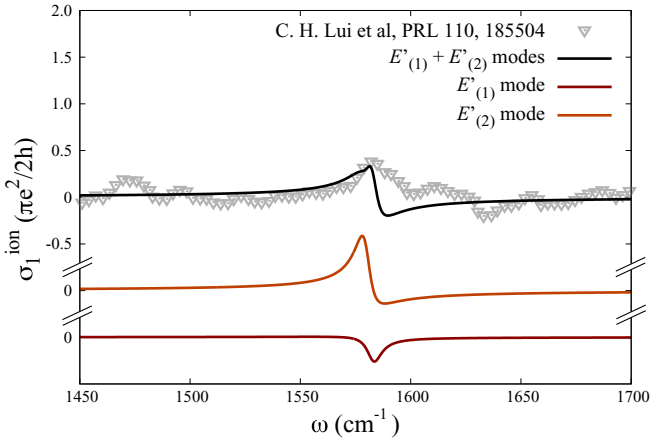

(a) Bernal (ABA) stacking

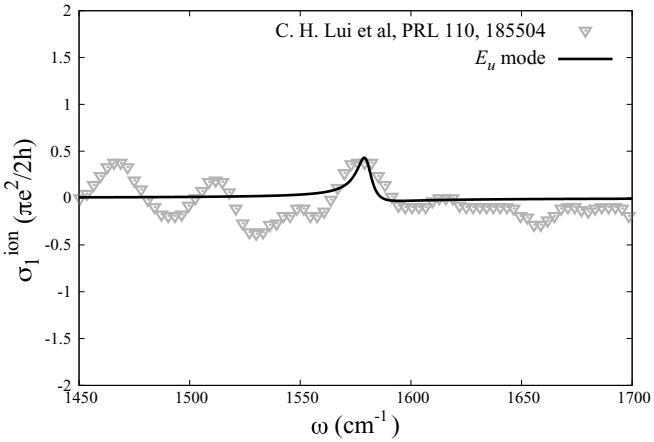

(b) Rhombohedral (ABC) stacking

FIG. 3. Comparison between simulated (continuous lines) and experimental (dots) real part of the conductivity, from Ref. [43]. In (a) we show, together with the total $\sigma_1^{\rm ion}$ (black), also the two contributions arising from the $E'_{(1)}$ (dark red) and $E'_{(2)}$ (orange) modes.

ionic conductivity by the relation $\boldsymbol{\sigma}^{\rm ion}(\omega) = -i\omega\boldsymbol{\chi}^{\rm ion}(\omega)$. As $\boldsymbol{\chi}^{\rm ion}(\omega)$, also $\boldsymbol{\sigma}^{\rm ion}(\omega)$ is composed of a sum over IR optical modes, as shown in Ref. [17]. In Fig. 3, we upshifted all the peaks of $\approx$20 cm^{-1}—that is, 1% of the NA phonon frequencies computed for the trilayers in Table IV—keeping the calculated *ab initio* splittings of the IR $E'_{(1)}$, $E'_{(2)}$ modes shown in Fig. 3(a). Notably, such IR modes have an almost opposite shape; when they are summed up, $\sigma_{\parallel}^{\rm ion}(\omega \simeq 0.2\ \text{eV}) \approx \sigma_{\parallel,E'_{(1)}}^{\rm ion} + \sigma_{\parallel,E'_{(2)}}^{\rm ion}$, the interference effect among them decreases the overall IR intensity, which agrees better with the experimental data. Furthermore, we find that nonadiabatic renormalization effects, albeit small, may affect the splitting of the in-plane modes of trilayer graphene in a detectable way (e.g., by high-resolution Raman spectroscopy).

We observe that the comparison of both bilayer and trilayer graphene with the experiments of Refs. [21,43] is done for the zero-doping case. In the same articles, the authors studied also the case of finite doping ϱ, finding a substantial enhancement of the same IR peaks by increasing/decreasing the total number of electrons. We also mention an experimental study of the same IR resonance as a function of the number of graphene layers [44], which, however, has been carried out with small unintentional doping levels. Although an analysis of the same peaks as a function of ϱ would be interesting, it is beyond the scope of this article, but it may be investigated in further studies.

IV. CONCLUSIONS

In conclusion, we introduced an *ab initio* scheme to describe the IR vibrational spectra of metallic crystalline solids in reflectivity measurements. We benchmarked our method by calculating the phonon signatures in the reflectivity spectra of graphite, finding good agreement between our results and available experimental data. We believe that our work will allow for a reliable first-principles description of reflectance spectra in metallic systems, in particular for those systems under extremely high-pressure conditions, as the new superconducting hydrides, where the IR vibrational spectroscopy represents one of the few possible tools of investigation.

ACKNOWLEDGMENTS

We acknowledge Alexey Kuzmenko for sharing the in-plane data of reflectivity, and Michele Ortolani and Leonetta Baldassarre for a critical reading and useful suggestions. We also acknowledge financial support by the European Graphene Flagship Core 2 and Core 3 and the CINECA award under the ISCRA initiative (Grants No. HP10BSZ6LY and No. HP10BKBJMI) for the availability of high-performance computing resources.

APPENDIX A: EXPANSION OF REFLECTIVITY

The expansion of the reflectivity for $4\pi|\chi^{\rm I}_{s,\alpha}| \ll |\epsilon^{\rm e}_{s,\alpha}|$ is obtained by approximating

$$\sqrt{\epsilon_{s,\alpha}} = \sqrt{\epsilon^{\rm e}_{s,\alpha} + 4\pi\,\chi^{\rm I}_{s,\alpha}} \sim \sqrt{\epsilon^{\rm e}_{s,\alpha}} + \frac{1}{2}\frac{4\pi\,\chi^{\rm I}_{s,\alpha}}{\sqrt{\epsilon^{\rm e}_{s,\alpha}}}, \tag{A1}$$

$$R_{s,\alpha} = \left|\frac{\sqrt{\epsilon_{s,\alpha}}-1}{\sqrt{\epsilon_{s,\alpha}}+1}\right|^2 \sim \left|\frac{\sqrt{\epsilon^{\rm e}_{s,\alpha}}-1}{\sqrt{\epsilon^{\rm e}_{s,\alpha}}+1}\right|^2 \left|1 + \frac{4\pi\,\chi^{\rm I}_{s,\alpha}}{\sqrt{\epsilon^{\rm e}_{s,\alpha}}\left(\epsilon^{\rm e}_{s,\alpha}-1\right)}\right|^2. \tag{A2}$$

The expression given in Eq. (3) of the main text is recovered by setting $R^{\rm e}_{s,\alpha} = \left|\frac{\sqrt{\epsilon^{\rm e}_{s,\alpha}}-1}{\sqrt{\epsilon^{\rm e}_{s,\alpha}}+1}\right|^2$ and neglecting again the quadratic term in the ratio $\frac{4\pi|\chi^{\rm I}_{s,\alpha}|}{|\epsilon^{\rm e}_{s,\alpha}|}$. For ω close to ω_s, this gives the expression of Eq. (3),

$$R_{s,\alpha}(\omega) = R^{\rm e}_{s,\alpha}\left[1 + 2\,\mathrm{Re}\left(\frac{4\pi\,\chi^{\rm I}_{s,\alpha}(\omega)}{\sqrt{\epsilon^{\rm e}_{s,\alpha}}\left(\epsilon^{\rm e}_{s,\alpha}-1\right)}\right)\right]. \tag{A3}$$

APPENDIX B: IMPLEMENTATION

In this Appendix, we describe the technical details regarding the practical implementation of the effective charge tensor and electronic susceptibility within QUANTUM ESPRESSO [35,36].

Neglecting the imaginary part of the induced charge density, the expression of the approximate frequency-dependent effective charge tensor can be written as [23]

$$
\begin{aligned}
e\boldsymbol{Z}^{\mathrm{e}}_{\kappa}(\omega_s) = &-\frac{1}{N_{\mathbf{k}}}\sum_{\mathbf{k},nm}\sum_{\zeta=\pm}\frac{f_{\mathbf{k},n}-f_{\mathbf{k},m}}{E_{\mathbf{k},n}-E_{\mathbf{k},m}+\zeta z_s}\\
&\times\langle u_{\mathbf{k},m}|\,\mathcal{V}^{\mathbf{E}}_{\mathrm{Re}}(\omega_s)|u_{\mathbf{k},n}\rangle\langle u_{\mathbf{k},n}|\,\mathcal{V}^{\mathbf{u}_\kappa}_{\mathrm{Re}}(\omega_s)|u_{\mathbf{k},m}\rangle\\
&+\frac{1}{\Omega}\int d^3r\,d^3r'\,\mathrm{Re}\,n^{\mathbf{E}}(\mathbf{r},\omega_s)\,K_{\mathrm{Hxc}}(\mathbf{r},\mathbf{r}')\\
&\times\,\mathrm{Re}\,n^{\mathbf{u}_\kappa}(\mathbf{r}',\omega_s),
\end{aligned}
\tag{B1}
$$

where $\mathcal{V}^{\boldsymbol{\xi}}_{\mathrm{Re}}(\omega)=V^{\boldsymbol{\xi}}_{\mathrm{KS}}[\mathrm{Re}\,n^{\boldsymbol{\xi}}(\omega)]$, in which $V^{\boldsymbol{\xi}}_{\mathrm{KS}}(\omega)$ is the Kohn-Sham potential, i.e., the sum of the external and the Hxc potentials, perturbed with respect to a perturbation depending parametrically on $\boldsymbol{\xi}$. Note that $\mathcal{V}^{\boldsymbol{\xi}}_{\mathrm{Re}}(\omega)=\mathcal{V}^{\boldsymbol{\xi}}_{\mathrm{Re}}(-\omega)$ is a Hermitian operator, contrary to $V^{\boldsymbol{\xi}}_{\mathrm{KS}}$, which instead satisfies $V^{\boldsymbol{\xi}}_{\mathrm{KS}}(\omega)^{\dagger}=V^{\boldsymbol{\xi}}_{\mathrm{KS}}(-\omega)$.

We rewrite the expression of the approximate effective charge tensor in the following way:

$$
\begin{aligned}
e\boldsymbol{Z}^{\mathrm{e}}_{\kappa}(\omega_s) = &-\frac{1}{N_{\mathbf{k}}}\sum_{\mathbf{k},n}\sum_{\zeta=\pm}\langle u_{\mathbf{k},n}|\,\mathcal{V}^{\mathbf{E}}_{\mathrm{Re}}(\omega_s)\,\mathcal{Q}|u^{\mathbf{u}_\kappa}_{\mathbf{k},n,\zeta}(\omega_s)\rangle\\
&+\frac{1}{\Omega_s}\int d^3r\,\mathcal{V}^{\mathbf{E}}_{\mathrm{Re}}(\mathbf{r},\omega_s)\,\mathrm{Re}\,n^{\mathbf{u}_\kappa}(\mathbf{r},\omega_s),
\end{aligned}
\tag{B2}
$$

where the sum over the band index n can be restricted to the states with non-negligible occupations. The first-order expression of the wave function is

$$
\begin{aligned}
\mathcal{Q}\big|u^{\mathbf{u}_\kappa}_{\mathbf{k},n,\zeta}(\omega_s)\big\rangle = &\sum_{m}\frac{f_{\mathbf{k},n}-f_{\mathbf{k},m}}{E_{\mathbf{k},n}-E_{\mathbf{k},m}+\zeta z_s}\\
&\times\langle u_{\mathbf{k},m}|\,\mathcal{V}^{\mathbf{u}_\kappa}_{\mathrm{Re}}(\omega_s)|u_{\mathbf{k},n}\rangle\,|u_{\mathbf{k},m}\rangle
\end{aligned}
\tag{B3}
$$

and the sum over m can be restricted to states with negligible occupations, within which $\mathcal{Q}$ is the projector. We can divide this last space into two subspaces: a subspace whose energy bands are resonant with the frequency (i.e., for which there are two or more energies satisfying $E_{\mathbf{k},m}-E_{\mathbf{k},n}=\omega_s$) and a subspace whose energies are nonresonant with the electronic transitions (i.e., $E_{\mathbf{k},m}-E_{\mathbf{k},n}\neq\omega_s$ for every m and n). In the former, a nonzero value of η is necessary in order to avoid a divergent integrand, whereas in the latter it can be set $\eta=0$ since in this case, $E_{\mathbf{k},n}-E_{\mathbf{k},m}\pm\omega_s\gg\pm\eta$ for every n, m, and $\mathbf{k}$. The components of $|u^{\mathbf{u}_\kappa}_{\mathbf{k},n,\zeta}(\omega_s)\rangle$, which are resonant with ω_s, can be treated by performing explicitly the sum in Eq. (B3), while all of the other components (relative to the infinite-dimensional manifold of nonresonant states) can be computed by means of the Sternheimer equation [45] with the same strategy of Refs. [15,46]. In this way, the first-order wave function can be obtained by

$$
\begin{aligned}
\mathcal{R}\big|u^{\mathbf{u}_\kappa}_{\mathbf{k},n,\zeta}(\omega_s)\big\rangle = &\sum_{m}\frac{f_{\mathbf{k},n}-f_{\mathbf{k},m}}{E_{\mathbf{k},n}-E_{\mathbf{k},m}+\zeta z_s}\\
&\times\langle u_{\mathbf{k},m}|\,\mathcal{V}^{\mathbf{u}_\kappa}_{\mathrm{Re}}|u_{\mathbf{k},n}\rangle\,|u_{\mathbf{k},m}\rangle,
\end{aligned}
\tag{B4}
$$

$$
\begin{aligned}
&(e^{-i\mathbf{k}\cdot\mathbf{r}}H_0e^{i\mathbf{k}\cdot\mathbf{r}}-E_{\mathbf{k},n}-\zeta\omega_s)\,\mathcal{S}\big|u^{\mathbf{u}_\kappa}_{\mathbf{k},n,\zeta}(\omega_s)\big\rangle\\
&\qquad=-f(E_{\mathbf{k},n})\,\mathcal{S}\,\mathcal{V}^{\mathbf{u}_\kappa}_{\mathrm{Re}}|u_{\mathbf{k},n}\rangle,
\end{aligned}
\tag{B5}
$$

in which $\mathcal{Q}=\mathcal{R}+\mathcal{S}$; $\mathcal{R}$ is the projector onto resonant states and $\mathcal{S}$ is the projector onto the nonresonant subspace. Note that, with this scheme, $\mathrm{Im}\,\boldsymbol{Z}^{\mathrm{e}}_{\kappa}$ embodies only contributions coming from resonant states.

The treatment for $\boldsymbol{\epsilon}^{\mathrm{e}}(\omega_s)$ is similar to that for $\boldsymbol{Z}^{\mathrm{e}}_{\kappa}(\omega_s)$, with the only difference being that, contrary to the effective charge tensor, it contains also a term corresponding to electronic intraband transitions, which at $\omega\to0$ manifests in the Drude peak. Therefore, we separate $\boldsymbol{\epsilon}^{\mathrm{e}}(\omega_s)=\boldsymbol{\epsilon}^{\mathrm{e}}_{\mathrm{inter}}(\omega_s)+\boldsymbol{\epsilon}^{\mathrm{e}}_{\mathrm{intra}}(\omega_s)$; $\boldsymbol{\epsilon}^{\mathrm{e}}_{\mathrm{inter}}(\omega_s)$ is calculated with the same methodology of $\boldsymbol{Z}^{\mathrm{e}}_{\kappa}(\omega_s)$, and

$$
\begin{aligned}
\boldsymbol{\epsilon}^{\mathrm{e}}_{\mathrm{intra}}(\omega_s) = &\frac{8\pi(e\hbar)^2}{N_{\mathbf{k}}\Omega}\sum_{\mathbf{k},nm}\left.\frac{df(x)}{dx}\right|_{x=E_{\mathbf{k},n}}\\
&\times\frac{\langle u_{\mathbf{k},n}|\mathbf{v}_{\mathbf{k}}|u_{\mathbf{k},m}\rangle\,\langle u_{\mathbf{k},m}|\mathbf{v}_{\mathbf{k}}|u_{\mathbf{k},n}\rangle}{\omega_s^2-\eta_s^2+i2\omega_s\eta_s}
\end{aligned}
\tag{B6}
$$

is computed explicitly, summing over the occupied and the resonant bands.

APPENDIX C: BRILLOUIN ZONE SAMPLING

Graphite is characterized by a density of states that decreases dramatically at the Fermi level. Because of its particular geometry of the band structure, it turns out that for a frequency-dependent response function, like the effective charges or the electric susceptibility, most of the contributions to the $\mathbf{k}$-point sum come from a small cylinder along the **K**-**H** line, in which the denominator of Eq. (B1) reaches its minimum value. Because of the very steep variation of the integrand around this region, an ultradense $\mathbf{k}$-point grid is necessary to have a well-converged result; for this purpose, we employed a nonuniform $\mathbf{k}$-points mesh in the (k_x,k_y) plane of the Brillouin zone (BZ). Since the (k_x,k_y) projection of the time-reversal-symmetrized BZ (TRS-BZ) of the hexagonal lattice is an equilateral triangle centered at **K**, we generate the grid in the following way: starting from one point at the center of the triangle, we defined various levels of $\mathbf{k}$-point densities; at the first level, from the point at the center of the BZ, we generated three points, each of them at the midpoint of the segment between the central point and one of the edges of the triangle. In this way, all four points can be considered to be each of them at the center of a smaller triangle, whose area is 1/4 of the area of the (k_x,k_y) TRS-BZ. The iteration of this procedure from all four points produces 4^2 points whose weight $w_{\mathbf{k}}$ is $1/4^2$; this defines the second level. At the ℓth level, the number of $\mathbf{k}$-points is 4^{ℓ}, and $w_{\mathbf{k}}=1/4^{\ell}$. To find the way in which the point should concentrate around the **K**-**H** line, i.e., $\ell=\ell_{\mathbf{k}}$, we required that, for a sum $\sum_{\mathbf{k}}w_{\mathbf{k}}\,I_{\mathbf{k}}$,

$$
4^{-\ell_{\mathbf{k}}}I_{\mathbf{k}}=C,
\tag{C1}
$$

where C is a constant. Assuming that, far from **K**, $I_{\mathbf{k}}\sim|\mathbf{k}-\mathbf{K}|^{-p}$, the density of $\mathbf{k}$-points (which is fixed by ℓ) at the distance $\mathcal{K}_{\mathbf{K}}=|\mathbf{k}-\mathbf{K}|$ must be

$$
\mathcal{K}_{\mathbf{K}}(\ell)=C'\,4^{-\ell/p}.
\tag{C2}
$$

Defining L as the max value of ℓ, we fixed the constant C' imposing $\mathcal{K}_{\mathbf{K}}(L)=D/\mathcal{N}$, where $\mathcal{N}$ is an integer and $D=4\pi/(3a)$ is the distance from **K** to an edge of a triangle; we choose $p=3$, according to the expression of $\mathrm{Re}\,\mathbf{Z}_{\kappa}(\omega)$ of the model in Ref. [17]; this choice is motivated by the fact that

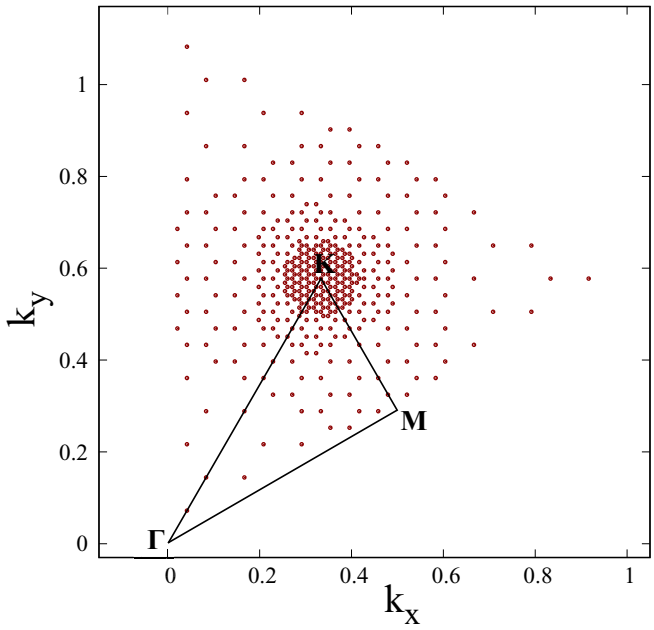

FIG. 4. Top view of time-reversal symmetrized mesh used for the integration within the BZ. The highlighted region is the irreducible 2D wedge, which is the only part used for the **k**-point sums. This figure is obtained using $L = 6$, $l = 3$, $\mathcal{N} = 8$, and, only for this figure, $p = 2.1$.

the linear-response calculation is carried out with $\mathrm{Re}\, n^{\xi}$. As a result,

$$\mathcal{K}_{\mathbf{K}}(\ell; L, l, \mathcal{N}) = \left(\frac{D}{\mathcal{N}}\right) 4^{(L-\ell)/3}, \tag{C3}$$

where $\ell \in \{L, L-1, \ldots, l+1, l\}$. The distance $\mathcal{K}_{\mathbf{K}}$ depends parametrically on L, l, and $\mathcal{N}$, which must be seen as parameters over which convergence tests must be made. We reported in Fig. 4 an example of the nonuniform grid.

For the calculations we used $(L, l, \mathcal{N}) = (9, 4, 25)$ and 90 N_{k_z} for $\boldsymbol{Z}^{\mathrm{e}}_{\kappa}(\omega_s)$, and $(L, l, \mathcal{N}) = (10, 4, 25)$ and 110 N_{k_z} for $\boldsymbol{\epsilon}^{\mathrm{e}}(\omega_s)$; these are equivalent, within the circle of radius $D/\mathcal{N}$, to a $724 \times 724 \times 90$ and a $1448 \times 1448 \times 110$ **k**-point grid, respectively.

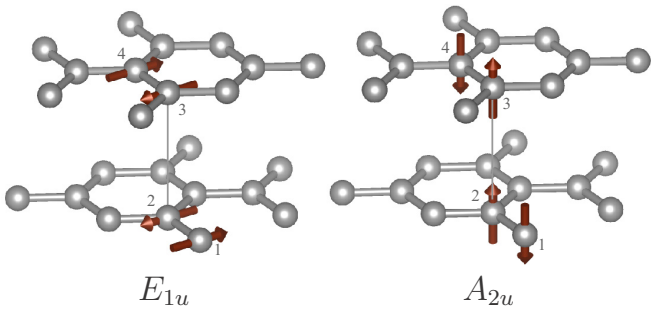

FIG. 5. IR-active modes of graphite.

TABLE V. Dependence on η of $\boldsymbol{Z}_{\kappa}(\omega_s)$ and $\boldsymbol{\epsilon}^{\mathrm{e}}(\omega_s)$ for $s = E_{1u}$ (up) and $s = A_{2u}$ (down).

η (10^{-3} Ry)	$\mathrm{Re}\, Z_{1,\parallel}$	$\mathrm{Re}\, Z_{2,\parallel}$	$\mathrm{Im}\, Z_{1,\parallel}$	$\mathrm{Im}\, Z_{2,\parallel}$	$\mathrm{Re}\, \epsilon^{\mathrm{e}}_{\parallel}$	$\mathrm{Im}\, \epsilon^{\mathrm{e}}_{\parallel}$
1	−0.268	0.269	−0.112	0.082	7.92	59.2
2	−0.270	0.273	−0.105	0.075	11.5	59.3
4	−0.267	0.276	−0.095	0.064	18.5	58.2
6	−0.263	0.276	−0.087	0.054	25.1	55.3
8	−0.258	0.276	−0.080	0.046	30.4	51.1
η (10^{-3} Ry)	$\mathrm{Re}\, Z_{1,\perp}$	$\mathrm{Re}\, Z_{2,\perp}$	$\mathrm{Im}\, Z_{1,\perp}$	$\mathrm{Im}\, Z_{2,\perp}$	$\mathrm{Re}\, \epsilon^{\mathrm{e}}_{\perp}$	$\mathrm{Im}\, \epsilon^{\mathrm{e}}_{\perp}$
0.5	−0.072	0.068	−0.00018	0.00002	3.44	0.710
1	−0.072	0.068	−0.00022	0.00001	3.44	0.791
2	−0.072	0.068	−0.00031	0.00000	3.51	0.906
3	−0.072	0.068	−0.00039	−0.00001	3.62	0.970
4	−0.072	0.068	−0.00047	−0.00002	3.73	0.980

APPENDIX D: η DEPENDENCE

We considered the dependence of both $\boldsymbol{Z}_{\kappa}(\omega_s)$ and $\boldsymbol{\epsilon}^{\mathrm{e}}(\omega_s)$ as a function of the parameter η. This parameter represents the inverse electronic lifetime, and it can be reasonably supposed to increase with temperature, because of the increase with T of both the electron-phonon and the electron-electron scattering processes.

We show in Fig. 5 the two IR-active modes of graphite. By symmetry, the effective charges of the two C atoms labeled by 2 and 3 are exactly equal, as well as the charges of the two 1 and 4 C atoms. The oscillator strength $\mathbf{d}_s(\omega_s)$ is obtained by taking the semidifference of $\boldsymbol{Z}_{\kappa}(\omega_s)$ and renormalizing by the square root of the number of atoms in the cell. In Table V we report the results of the calculations. The effective charge and the electronic dielectric tensors are both computed at $T = 300$ K, with $a = 2.46$ Å and $c = 6.70$ Å. All the other parameters (e.g., cutoff, **k**-point mesh, and so on) are the same as the previous calculations. It is found that $\mathrm{Im}\, Z_{\kappa,\parallel}$ decreases with the increase of η; this fact suggests agreement with the experimental observation of the decrease of this quantity with the increase of T.

For the sake of completeness, we also report the numerical values for the effective charges at $T = 150$ K evaluated with

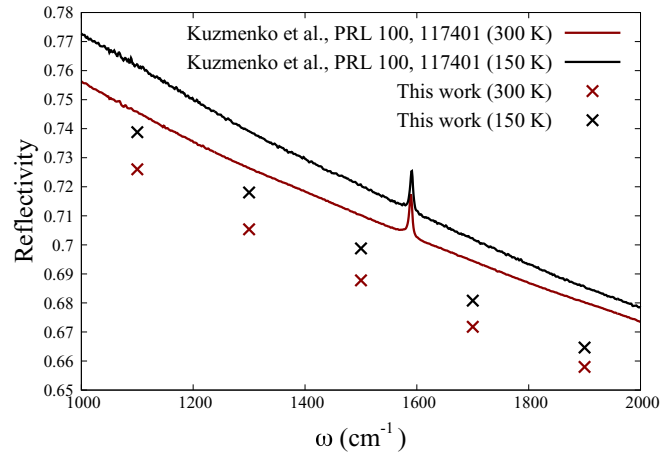

FIG. 6. Frequency dependence of $R^{\mathrm{e}}_{s,\alpha}$ in Eq. (A3).

lattice constant $c = 6.68$ Å to account for the thermal compression, while keeping the in-plane lattice constant fixed at $a = 2.46$ Å [39]:

$$Z_{1,\parallel}(\eta = 10^{-3}\,\mathrm{Ry}) = -(0.267 + i0.110),$$
$$Z_{2,\parallel}(\eta = 10^{-3}\,\mathrm{Ry}) = (0.270 + i0.079),$$
$$Z_{1,\perp}(\eta = 5 \times 10^{-4}\,\mathrm{Ry}) = -(0.073 + i0.00021),$$
$$Z_{2,\perp}(\eta = 5 \times 10^{-4}\,\mathrm{Ry}) = (0.071 + i0.00002).$$

Overall, all considered quantities do not show significant dependences on thermal expansion, whereas they depend more markedly on the damping parameter η.

APPENDIX E: DIELECTRIC TENSOR WITHIN IR RANGE

In this Appendix, we show the results of our calculation of the frequency-dependent dielectric tensor in a wider range of IR spectrum. Using $\eta_{E_{1u}} = 110\ \mathrm{cm}^{-1}$ and the same input files as for the previous computations, we calculated the electronic dielectric tensor from 1100 to 1900 cm^{-1}. We then evaluated $R^{\mathrm{e}}_{E_{1u},\parallel}$ using the computed $\epsilon^{\mathrm{e}}_{\parallel}(\omega_{E_{1u}})$.

We show in Fig. 6 the results of our calculations, compared to the experimental measurements of reflectivity of Ref. [30]. The calculated and the experimental $R^{\mathrm{e}}_{E_{1u},\parallel}$, besides having the same ω-dependence, also display a very similar dependence on temperature, which becomes less important at larger frequencies.

[1] P. Brüesch, *Phonons. Theory and Experiments: Part II.*, Springer Series in Solid-State Sciences (Springer-Verlag, Berlin, Heidelberg, 1986).
[2] T. Timusk and B. Statt, Rep. Prog. Phys. **62**, 61 (1999).
[3] B. Ruzicka, L. Degiorgi, H. Berger, R. Gaál, and L. Forró, Phys. Rev. Lett. **86**, 4136 (2001).
[4] S. V. Borisenko, A. A. Kordyuk, A. N. Yaresko, V. B. Zabolotnyy, D. S. Inosov, R. Schuster, B. Büchner, R. Weber, R. Follath, L. Patthey, and H. Berger, Phys. Rev. Lett. **100**, 196402 (2008).
[5] Y. Umemoto, K. Sugawara, Y. Nakata, T. Takahashi, and T. Sato, Nano Res. **12**, 165 (2018).
[6] L. Baldassarre, A. Perucchi, D. Nicoletti, A. Toschi, G. Sangiovanni, K. Held, M. Capone, M. Ortolani, L. Malavasi, M. Marsi, P. Metcalf, P. Postorino, and S. Lupi, Phys. Rev. B **77**, 113107 (2008).
[7] S. J. Moon, Y. S. Lee, A. A. Schafgans, A. V. Chubukov, S. Kasahara, T. Shibauchi, T. Terashima, Y. Matsuda, M. A. Tanatar, R. Prozorov, A. Thaler, P. C. Canfield, S. L. Bud'ko, A. S. Sefat, D. Mandrus, K. Segawa, Y. Ando, and D. N. Basov, Phys. Rev. B **90**, 014503 (2014).
[8] A. P. Drozdov, M. I. Eremets, I. A. Troyan, V. Ksenofontov, and S. I. Shylin, Nature (London) **525**, 73 (2015).
[9] F. Capitani, B. Langerome, J.-B. Brubach, P. Roy, A. Drozdov, M. I. Eremets, E. J. Nicol, J. P. Carbotte, and T. Timusk, Nat. Phys. **13**, 859 (2017).
[10] A. P. Drozdov, P. P. Kong, V. S. Minkov, S. P. Besedin, M. A. Kuzovnikov, S. Mozaffari, L. Balicas, F. F. Balakirev, D. E. Graf, V. B. Prakapenka, E. Greenberg, D. A. Knyazev, M. Tkacz, and M. I. Eremets, Nature (London) **569**, 528 (2019).
[11] M. Somayazulu, M. Ahart, A. K. Mishra, Z. M. Geballe, M. Baldini, Y. Meng, V. V. Struzhkin, and R. J. Hemley, Phys. Rev. Lett. **122**, 027001 (2019).
[12] M. I. Eremets, A. P. Drozdov, P. P. Kong, and H. Wang, Nat. Phys. **15**, 1246 (2019).
[13] C. Ji, B. Li, W. Liu, J. S. Smith, A. Majumdar, W. Luo, R. Ahuja, J. Shu, J. Wang, S. Sinogeikin, Y. Meng, V. B. Prakapenka, E. Greenberg, R. Xu, X. Huang, W. Yang, G. Shen, W. L. Mao, and H.-K. Mao, Nature (London) **573**, 558 (2019).
[14] E. K. U. Gross and W. Kohn, Phys. Rev. Lett. **55**, 2850 (1985).
[15] S. Baroni, S. de Gironcoli, A. Dal Corso, and P. Giannozzi, Rev. Mod. Phys. **73**, 515 (2001).
[16] M. Born and K. Huang, *Dynamical Theory of Crystal Lattices*, Oxford Classic Texts in the Physical Sciences (Clarendon, Oxford, 1988).
[17] O. Bistoni, P. Barone, E. Cappelluti, L. Benfatto, and F. Mauri, 2D Mater. **6**, 045015 (2019).
[18] E. Cappelluti, L. Benfatto, M. Manzardo, and A. B. Kuzmenko, Phys. Rev. B **86**, 115439 (2012).
[19] U. Fano, Phys. Rev. **124**, 1866 (1961).
[20] R. Nemanich, G. Lucovsky, and S. Solin, Solid State Commun. **23**, 117 (1977).
[21] A. B. Kuzmenko, L. Benfatto, E. Cappelluti, I. Crassee, D. van der Marel, P. Blake, K. S. Novoselov, and A. K. Geim, Phys. Rev. Lett. **103**, 116804 (2009).
[22] X. Gonze and C. Lee, Phys. Rev. B **55**, 10355 (1997).
[23] M. Calandra, G. Profeta, and F. Mauri, Phys. Rev. B **82**, 165111 (2010).
[24] W. Kohn and L. J. Sham, Phys. Rev. **140**, A1133 (1965).
[25] F. Giustino, M. L. Cohen, and S. G. Louie, Phys. Rev. B **81**, 115105 (2010).
[26] M. Manzardo, E. Cappelluti, E. van Heumen, and A. B. Kuzmenko, Phys. Rev. B **86**, 054302 (2012).
[27] C. Underhill, S. Leung, G. Dresselhaus, and M. Dresselhaus, Solid State Commun. **29**, 769 (1979).
[28] S. Leung, C. Underhill, G. Dresselhaus, and M. Dresselhaus, Solid State Commun. **33**, 285 (1980).
[29] H. R. Philipp, Phys. Rev. B **16**, 2896 (1977).
[30] A. B. Kuzmenko, E. van Heumen, F. Carbone, and D. van der Marel, Phys. Rev. Lett. **100**, 117401 (2008).
[31] R. J. Papoular and R. Papoular, Mon. Not. R. Astron. Soc. **443**, 2974 (2014).
[32] H. Venghaus, Phys. Status Solidi B **81**, 221 (1977).
[33] H. Venghaus, Phys. Status Solidi B **71**, 609 (1975).
[34] B. T. Draine, Astrophys. J. **831**, 109 (2016).
[35] P. Giannozzi, S. Baroni, N. Bonini, M. Calandra, R. Car, C. Cavazzoni, D. Ceresoli, G. L. Chiarotti, M. Cococcioni, I. Dabo, A. Dal Corso, S. de Gironcoli, S. Fabris, G. Fratesi, R. Gebauer, U. Gerstmann, C. Gougoussis, A. Kokalj, M. Lazzeri, L. Martin-Samos, N. Marzari, F. Mauri, R. Mazzarello, S. Paolini, A. Pasquarello, L. Paulatto, C. Sbraccia, S. Scandolo, G. Sclauzero, A. P. Seitsonen, A. Smogunov, P. Umari, and R. M. Wentzcovitch, J. Phys.: Condens. Matter **21**, 395502 (2009).

[36] P. Giannozzi, O. Andreussi, T. Brumme, O. Bunau, M. B. Nardelli, M. Calandra, R. Car, C. Cavazzoni, D. Ceresoli, M. Cococcioni, N. Colonna, I. Carnimeo, A. D. Corso, S. de Gironcoli, P. Delugas, R. A. DiStasio, A. Ferretti, A. Floris, G. Fratesi, G. Fugallo, R. Gebauer, U. Gerstmann, F. Giustino, T. Gorni, J. Jia, M. Kawamura, H.-Y. Ko, A. Kokalj, E. Küçükbenli, M. Lazzeri, M. Marsili, N. Marzari, F. Mauri, N. L. Nguyen, H.-V. Nguyen, A. O. de-la Roza, L. Paulatto, S. Poncé, D. Rocca, R. Sabatini, B. Santra, M. Schlipf, A. P. Seitsonen, A. Smogunov, I. Timrov, T. Thonhauser, P. Umari, N. Vast, X. Wu, and S. Baroni, J. Phys.: Condens. Matter **29**, 465901 (2017).

[37] D. M. Ceperley and B. J. Alder, Phys. Rev. Lett. **45**, 566 (1980).

[38] N. Troullier and J. L. Martins, Phys. Rev. B **43**, 1993 (1991).

[39] J. C. Boettger, Phys. Rev. B **55**, 11202 (1997).

[40] G. S. Jeon and G. D. Mahan, Phys. Rev. B **71**, 184306 (2005).

[41] P. Giura, N. Bonini, G. Creff, J. B. Brubach, P. Roy, and M. Lazzeri, Phys. Rev. B **86**, 121404(R) (2012).

[42] A. M. Saitta, M. Lazzeri, M. Calandra, and F. Mauri, Phys. Rev. Lett. **100**, 226401 (2008).

[43] C. H. Lui, E. Cappelluti, Z. Li, and T. F. Heinz, Phys. Rev. Lett. **110**, 185504 (2013).

[44] Z. Li, C. H. Lui, E. Cappelluti, L. Benfatto, K. F. Mak, G. L. Carr, J. Shan, and T. F. Heinz, Phys. Rev. Lett. **108**, 156801 (2012).

[45] R. M. Sternheimer, Phys. Rev. **96**, 951 (1954).

[46] S. Baroni, P. Giannozzi, and A. Testa, Phys. Rev. Lett. **58**, 1861 (1987).